

In Situ Observations of Nanoparticle Early Development Kinetics at Mineral–Water Interfaces

YOUNG-SHIN JUN,^{*,†} BYEONGDU LEE,[‡]
AND GLENN A. WAYCHUNAS[§]

Department of Energy, Environmental and Chemical Engineering, Washington University, St. Louis, Missouri 63130, United States, X-ray Science Division, Argonne National Laboratory, Argonne, Illinois 60439, United States, and Earth Science Division, Geochemistry Department, Lawrence Berkeley National Laboratory, Berkeley, California 94720, United States

Received May 4, 2010. Revised manuscript received September 8, 2010. Accepted September 15, 2010.

The early development of nanoparticles at mineral–water interfaces exerts crucial influences on the sequestration and transport of aqueous toxic species originating from both natural and anthropogenic sources. Homogeneous and heterogeneous nucleation often occur simultaneously, making it difficult to sort out whether toxic species are transported as free species, sorbed on nanoparticle surfaces, or trapped between aggregated nanoparticles. Here, using a newly developed X-ray scattering setup, we show how homogeneous nucleation and growth can be quantitatively separated from heterogeneous processes under aqueous conditions in real-time. Under conditions found in acid-mine-drainage (at pH 3.6 and $[\text{Fe}^{3+}] = 10^{-4} \text{ M}$), heterogeneous nucleation of iron oxide nanoparticles on quartz dominated homogeneous nucleation by a factor of 192 (by particle volume). The smallest heterogeneously formed nanoparticles had radii of $1.7 \pm 0.5 \text{ nm}$, significantly smaller than the size estimated using classical nucleation theory (CNT). Based on the data, the dominant nucleation and growth mechanisms of iron oxide nanoparticles depending on ionic strength were presented. Our findings have implications for the formation and transport of nanoparticles, and thus toxins, in both environmental and biological systems.

Introduction

Predicting the fate and transport of toxic contaminants in environmental systems requires quantitative information about the early nucleation and growth of nanoparticles, both in solution and at mineral surfaces. The early stages of iron oxide nanoparticle formation can involve fast incorporation of toxic metals and anions into their structure matrix, as well as interactions with extracellular biogenic polymers (1) and proteins (2, 3). Both phenomena can often affect the metabolism of microbial communities in acid mine drainage (AMD) systems (3). Further, the sorption or growth of nanoparticles on mineral surfaces may control the existing mineral surface's reactivity and modify its ability to influence

contaminant transport by engaging in adsorption, exchange, and redox reactions (4). Strongly sorbed toxic species at bulk mineral surfaces can be relatively immobile. However, homogeneously formed nanoparticles can sorb or incorporate toxic metals and carry toxins downstream (5). Nanoparticles can also incorporate toxins by aggregation, a process that additionally may alter porosity and permeability in their flow channels (6). As homogeneous and heterogeneous nucleation and subsequent growth often occur simultaneously, the kinetics of these processes in their earliest stages are difficult to untangle, and hence the individual contributions are poorly defined. This problem is due to lack of suitable in situ real-time measurement tools that can quantify the nature of aqueous interfacial reactions with sufficient spatial and temporal resolution.

From the standpoint of environmental predictive modeling, a better mechanistic and kinetic understanding of metal (hydr)oxide precipitation at mineral–water interfaces is essential for accurate rate models of contaminant transport in soil and other microporous media. Kinetic studies of nucleation and growth of particles at mineral–water interfaces are usually performed via batch reactor experiments (7, 8). These approaches provide indirect kinetic information based only on changes in aqueous concentrations and on the number of particles suspended in solution, but do not allow direct quantification of nanometer scale processes or of accompanying aggregation phenomena. Although recent in situ atomic force microscopy studies have reported clues on the nature of nanofilm growth at water–carbonate interfaces (4, 9), generally nucleation stages and initial precipitate morphology at aqueous interfaces are not observable. Powerful imaging techniques such as transmission electron microscopy (TEM) and scanning electron microscopy (SEM) are limited by sample dehydration (10, 11), effectively undermining in situ character and eliminating the possibility of time-resolved studies (12). Recently, Pouget et al. reported in situ observation of template-controlled amorphous calcium carbonates using cryo-TEM (13), but could not distinguish heterogeneous from homogeneous nucleation. In addition, relevant *ab initio* calculations require good estimates of interfacial energies, the density of nucleation sites, and the free energy of critical nucleus formation, most of which are unavailable (12). Consequently, an accurate in situ determination of hydrated nanoparticle size, shape, and growth characteristics within the time frame of nuclei formation is crucial (10).

To address these issues, we have adapted small-angle X-ray scattering techniques—both transmission (SAXS) and grazing incidence (GISAXS) geometries (14, 15)—to study in situ nucleation and growth of iron oxide nanoparticles at quartz–water interfaces. For the first time, this study provides quantitative comparisons between heterogeneous and homogeneous nucleation and growth of nanoparticles from their critical nucleus sizes. It further yields direct observations of highly hydrous nanoparticle development as a function of aqueous conditions, a regime appropriate for AMD formation. This study provides more accurate depiction of evolving nanoparticle distributions and topology at an active interface without dehydration.

Experimental Section

In Situ Time-Resolved Simultaneous SAXS/GISAXS Measurements. In GISAXS setup, a low divergence incident X-ray beam is directed toward the substrate surface at a grazing angle α_i , which needs to be close to but smaller than the critical angle (α_c) of the substrate for the total external X-ray

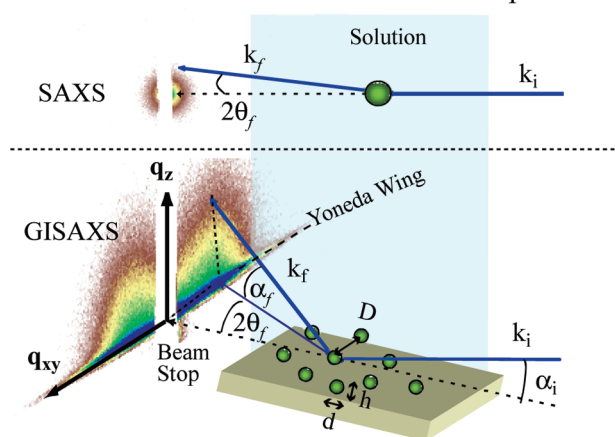
* Corresponding author phone: (314) 935-4539; fax: (314) 935-7211; e-mail: ysjun@seas.wustl.edu.

[†] Washington University.

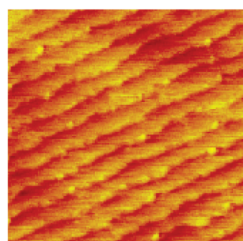
[‡] Argonne National Laboratory.

[§] Lawrence Berkeley National Laboratory.

A. Simultaneous SAXS/GISAXS setup



B. Clean quartz substrate (1 μm × 1 μm)



70-80 nm terrace
of stepped surface
(0.16-0.32 nm steps)

FIGURE 1. Heterogeneous nucleation and growth of iron oxide at water-quartz interfaces using in situ time-resolved simultaneous SAXS/GISAXS technique. (A) Simultaneous SAXS/GISAXS setup geometry. k_i and k_f are the incident and scattered wave vectors, α_i and α_f are the incident and exit scattered angles of the X-rays out of the surface plane, $2\theta_i$ is the exit angles of X-rays within the surface plane, D is the interparticle spacing ($\approx 2\pi/q_{xy}^*$, where q_{xy}^* is the q_{xy} at the center of the peak), and d ($= 2 R_{g,lateral}$) and h ($= 2 R_{g,vertical}$) are the diameter and height of nanoparticles, respectively. Scattering vector, q , is $k_i - k_f$. Each data point is measured with 10 s exposure time. (B) Clean (1010) surface of quartz by AFM measurements.

reflection so that X-ray beam will probe only structures on the substrate surface. The incident beam will be scattered by newly formed iron oxide nanoparticles on the surface, and this scattered intensity will be collected by the 2-D CCD detector (refer to Figure 1, refs 14 and 15, and references therein). The scattering intensity increases with the increase in the number and size of surface nanoparticles. When nanoparticles are spaced into an assembly, the broad Bragg diffraction peak associated to the nearest neighbor distance appears (see the theoretical formula in eq 1).

For in situ time-resolved simultaneous SAXS/GISAXS we used the following experimental parameters: 15 keV X-ray energy, a ~ 2 m sample to detector distance ($0.0085 \text{ \AA}^{-1} < q < 0.276 \text{ \AA}^{-1}$), $150 \mu\text{m}$ (V) \times 1 mm (H) beam size, 10 s exposure times, and an incidence angle, $\alpha_i = 0.09^\circ$ ($\alpha_c = 0.13^\circ$ and 99.2% reflectivity at 15 keV based on the calculations using ref 16). Strong diffuse scattering along α_f was blocked by installing a vertical beamstop. The cell has a 1 cm water path along the X-ray beam, which represents a trade-off between sufficiently transparency to the incident X-ray beam (22% transmission at 15 keV, respectively), and sufficient sample interface area (for signal strength). Experiments were done on beamline 12 IDC at the Advanced Photon Source, with earlier developmental testing at the Stanford Synchrotron Radiation Laboratory. The lateral and vertical nanoparticle sizes and interparticle spacings (D) on the quartz surfaces were extracted from the GISAXS images. Average radii and

the spacings of nanoparticles in bulk solution were determined from the SAXS data.

Substrate and Solution Sample Preparation. Clean (1010) surfaces of quartz were used as model reaction surfaces. The sample was a synthetically grown quartz plate of 1 mm thickness, cut along (1010) plane and polished by chemical/mechanical etching to near atomic-scale flatness (typical rms roughness about 2.5 \AA) (Figure 1B). Quartz surfaces are chosen because they are environmentally ubiquitous and have similar electrostatic characteristics to feldspars, clays, and several other silicate–water systems. As a model metal (hydr)oxide, iron oxides were selected for their abundance and significance in the fate and transport of environmental contaminants. Before every series of GISAXS measurements, the substrates were cleaned in a concentrated sulfuric acid solution mixed with a commercial oxidizing agent, Nochromix, for 3 h to remove organic contaminants, followed by thorough rinsing in distilled water and storage in microfiltered distilled water of circumneutral pH. Before sample measurement, the storage solution was removed by blow-drying with high purity nitrogen gas. For every experiment, new quartz samples were placed inside of a specially designed SAXS/GISAXS fluid cell and aligned with respect to the incoming X-ray direction. Once the samples were aligned, 10^{-4} M ferric solutions ($\text{Fe}(\text{NO}_3)_3$, JT Baker) at 1, 10, and 100 mM (adjusted by NaNO_3 , Mallinckrodt) ionic strength (IS) were introduced ($\text{pH } 3.6 \pm 0.2$). The ferric solution concentration was chosen for two reasons: one, it allows optimal conditions to observe the early nucleation and growth of iron oxides; and second, this particular concentration is found frequently in the environment (17, 18). From the moment the solution contacted with the substrates, the reactions were monitored; and the resulting particle scattering data, both within the solution and on the surface, were collected simultaneously.

Scattering Data Analysis. Standard SAXS image corrections such as the dark current subtraction have been applied prior to further data treatment. In both SAXS and GISAXS, the first scattering image for each time series was used to estimate background scattering (i.e., scattering from water, and dissolved ferric and nitrate ions) as initially (and for a well-defined prenucleation period) there was no discernible particle scattering component in the data images. For GISAXS data analysis, intensities of horizontal and vertical cuts are fitted with theoretical models in order to determine the lateral and vertical particle sizes ($R_{g,lateral}$ and $R_{g,vertical}$ in Figure 2), respectively, and additionally interparticle spacings when available. Line-cuts were made along the highest intensity; for horizontal cuts along the so-called Yoneda wing (14, 15) and for vertical cuts along the Bragg rod scattering, respectively. The Yoneda wing (at $\alpha_f \approx \alpha_c$ of the samples) results from the enhancement of the transmitted beam at the critical angle, which originates from the coherent coupling between the incident, reflected and transmitted X-ray fields at the surface (14, 19, 20).

Grazing incidence X-ray scattering (surface particle scattering) intensities, $I_{GISAXS,p}$, in our experiment are modeled with spherical particles as follows:

$$I_{GISAXS,p}(q) = I_{p1}(q) + I_{p2}(q) = I(0)_{p1} \times P_{p1}(q, R_1, \sigma_{R1}) \times S(q, D, \sigma_D) + I(0)_{p2} \times P_{p2}(q, R_2, \sigma_{R2}) \quad (1)$$

where $P(q, R, \sigma) = (\Delta\rho)^2 \int n(R, \sigma) \cdot V^2 (9(\sin(qR) - qR\cos(qR))^2 / ((qR)^6) dR$. p_1 and p_2 denote the large particle size at early stage nucleation and the small particles at later growth stage (in Figure 3C and D), respectively. The Schultz distribution function is used for the size distribution, $n(R, \sigma)$, of each particle. We included p_1 and p_2 because we observed the formation of small particles (0.8–1 nm radius) at the later growth stage of larger particles. The larger particles showed

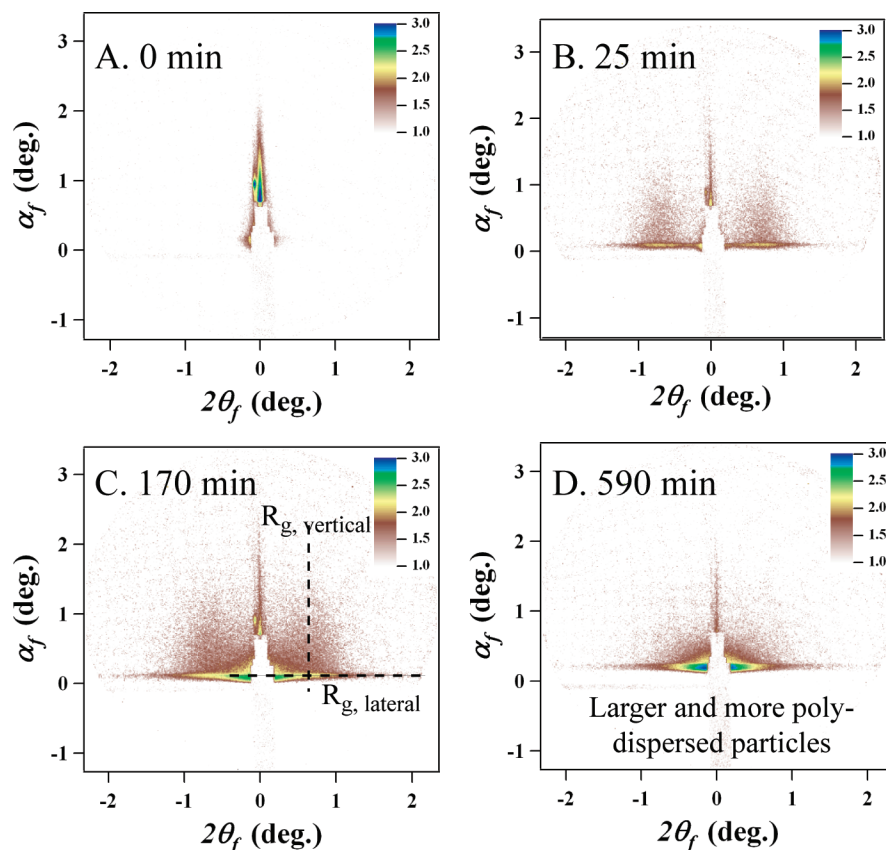


FIGURE 2. Time series of 2-D GISAXS images after exposure of quartz substrate to ferric solutions ($[\text{Fe}^{3+}] = 0.1 \text{ mM}$, $[\text{NaNO}_3] = 10 \text{ mM}$, and pH 3.6). The shift of the lobe location toward a smaller $2\theta_f$ indicates the growth of nanoparticles, and the disappearance of distinct lobes suggests particle coalescence. Iron oxide nuclei start to grow with well-defined interparticle spacing. Later, the nuclei coalesce, forming larger particles, and exhibit a more polydisperse distribution. This 2D data can be reduced to 1-D by cutting along the dotted lines in (C), and $2\theta_f$ is converted to q_{xy} in Figure 3 by the relationship of $q_{xy} = 4\pi/\lambda \sin((2\theta_f)/2)$.

interparticle distance peaks, which can be modeled by the paracrystal model and denoted as $S(q, D, \sigma_D)$ in eq 1, whereas smaller particles are well dispersed and therefore $S(q)$ is not required for them. Other parameters are $\Delta\rho$ is the difference of the scattering-length densities between the nanoparticles and solutions, V is the volume of each nanoparticles, R_1 and R_2 are the radii of p_1 (large particles) and p_2 (small particles), and $I(0)$ is the scattering intensity at $q = 0$ and this quantity is proportional to $(\Delta\rho)^2 \sum_i V_i^2$.

For large and randomly oriented nanoparticles or transmission SAXS, we use the Guinier approximation (eq 2) to calculate the particle sizes.

$$I_{\text{SAXS}}(q) = I_{\text{SAXS},p}(q) \approx I(0) \exp(-q^2 R_g^2/3) \quad (2)$$

where $I(0) = N_p(\Delta\rho)^2 V_p^2$. R_g is the radius of gyration (a root mean square distance of all elemental scattering volumes from the center of mass weighted by their scattering density). R_g of a particles is equal to $\sqrt{(3/5)R}$ for a spherical particle where R is the radius of the particle. All the fitting processes used the Igor pro program (V. 6.0, WaveMetrics, Inc., Oregon) with the GISAXS SHOP macro, which is available at the APS beamline 12 IDC.

Results and Discussion

By performing GISAXS and SAXS simultaneously using a specially designed fluid cell, we determined the nucleation density and progression as a function of ionic strength (IS) both on substrate surfaces and in the bulk water phase near the substrate. Quartz substrates exposed to 10^{-4} M ferric solution at 10 mM NaNO_3 IS presented no discernible particle

scattering during the initial 2–3 min. However, after 3 min, two identical scattering lobes developed. These lobes indicated both a well-defined spacing and size of surface-grown iron oxide nanoparticles. Subsequent nanoparticle growth was rapid laterally but not vertically (Figure 2). Eventually, nanoparticle coalescence occurred, but a continuous film did not form. The surface nanoparticle radii at different IS are shown in Figures 3 and 4. For all experimental cases, the nanoparticles in solutions were much larger ($R_{\text{IS}=10 \text{ mM}} = 16.9 \pm 0.6 \text{ nm}$; $R_{\text{IS}=100 \text{ mM}} = 11.5 \pm 0.7 \text{ nm}$) than those at the surface, but were far less abundant.

We note that homogeneously nucleated particles can also be collected at the quartz–water interface via gravitational settling. However, this contribution was negligible when tested by collecting SAXS/GISAXS data with the fluid cell inverted (Supporting Information Figure S1B). In a relatively short distance less than a micrometer scale, Brownian motion also can result in nanoparticle collection via collision with stationary surfaces (6), and nanoparticles could also be collected at the surface by DLVO forces (21). Based on classical nucleation theory (7) (and references therein), homogeneous nuclei initially should be larger than heterogeneous nuclei, and we observed at least a 2-fold size increase of solution-nucleated over surface-nucleated particles. If a collection mechanism is dominant, the particle size distribution should be bimodal (i.e., a larger particle size from the collection of particles from the solution, and a smaller particle size from heterogeneous nucleation at the surface). In the experimental data, however, bimodal particle size distribution of nucleation was not observed. Hence, collection

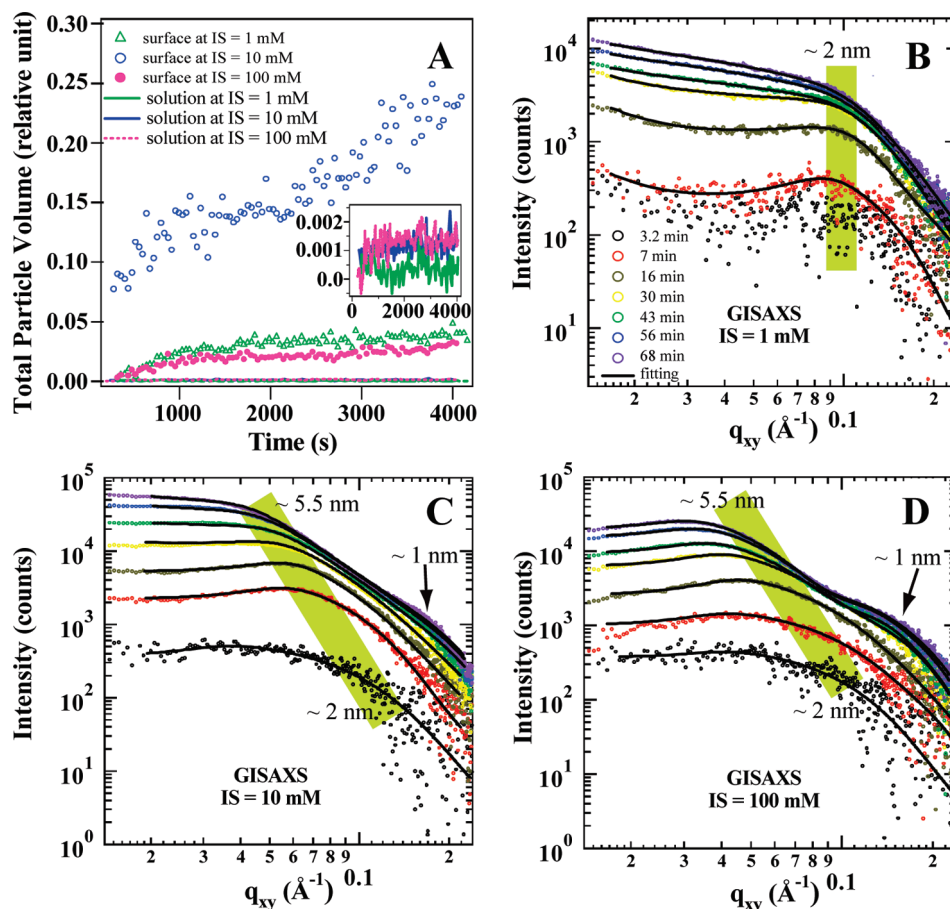


FIGURE 3. In situ simultaneous measurements of homogeneous nucleation and heterogeneous nucleation. (A) Quantitative comparison between homogeneously and heterogeneously nucleated total particle volumes under varied aqueous conditions. At $[\text{Fe}^{3+}] = 10^{-4}$ M at pH 3.6, heterogeneous nucleation is the dominant nucleation mechanism. The inset in (A) shows an enlarged diagram for homogeneously nucleated total particle volume; the axis labels are same as in (A). (B)–(D): In-plane GISAXS scattering at $q_z = 0.0224 \text{ \AA}^{-1}$ (around Yoneda wing, $\alpha_i = \text{critical angle of samples } (\alpha_c)$). Green strips and numbers depict the position of interparticle peaks and the approximate lateral radii of nanoparticles, respectively.

by any means cannot be a major mechanism of early stage surface nanoparticle formation. Therefore, we deduce that the particle scattering contributing to the GISAXS represents only heterogeneously nucleated nanoparticles, while the particle scattering contributing to the SAXS represents only homogeneously nucleated nanoparticles.

Quantitative Comparison between Homogeneously and Heterogeneously Formed Nanoparticles. The quantities of homogeneously and heterogeneously formed nanoparticles, in relative units, were calculated directly from the SAXS and GISAXS intensities (Figure 3A). Equation 2 suggests that $I_{\text{SAXS}}(0)/V_p$ equals to the total volumes of nanoparticles in solutions. The quantity is in theory identical to the so-called invariant ($Q = (1)/(2\pi^2) \int_0^\infty q^2 I(q) dq$). The SAXS invariant represents the integrated scattering intensity and is proportional to the total volume of nanoparticles irradiated by X-rays multiplied by the mean square of the electron density differences between nanoparticle and water (22). The same physical quantity could be obtained for the particles on substrate from GISAXS data, especially from horizontal line cuts, as long as GISAXS intensity is corrected for the signal enhancement factor $|\Psi_i(\alpha_i)|^2 |\Psi_f(\alpha_f)|^2$ due to the waveguiding effect. Since we made horizontal line cuts at $\alpha_i = \alpha_c$, it is more exactly $|\Psi_i(\alpha_i)|^2 |\Psi_f(\alpha_c)|^2$, which is the intensity of the Yoneda wing on top of broad particle scattering, and the factors for IS = 1, 10, and 100 mM are estimated to about 3.5, 3.1, and 2.9, respectively.

Based on the above calculations, the amount of homogeneously formed nanoparticles increased with increasing IS, and leveled off at 10 mM IS and above (Figure 3A). This trend was expected because greater IS decreases the electrostatic repulsive forces and allows cluster assembly into nanoparticles with perceptible electron density differences. For example, at IS = 10 mM in Figure 5, the Debye length (diffuse layer thickness, 2.96 nm) is similar to or smaller than the nanoparticle diameters. Hence, repulsive forces are insufficient to stop cluster assembly. In contrast, heterogeneously formed nanoparticles present significantly larger total particle volumes. The ratios of heterogeneously to homogeneously nucleated iron oxide nanoparticles after 4000 s reaction time were 83, 192, and 28 at IS = 1, 10, and 100 mM, respectively, indicating strong preference for heterogeneous nucleation (Figure 3A).

Nature of Iron Oxide Nanoparticles. The nature of the iron oxide nanoparticles at the surface can be inferred by thermodynamic calculations. The activity of ferric ions at different IS can vary considerably. To estimate effective Fe^{3+} activities and the degree of solution supersaturation with respect to ferrihydrite precipitation, we used $(\text{Fe}(\text{OH})_3)$, the simplest chemical formula of ferrihydrite and also one of the least stable iron oxides) (23). We used the modified Davies equation (24) $\log \gamma_{\text{Fe}^{3+}} = -A z^2 \times ((\sqrt{IS})/(1 + \sqrt{IS}) - 0.2IS)$, where $\gamma_{\text{Fe}^{3+}}$ is the activity coefficient, $\{\text{Fe}^{3+}\}(\text{activity}) = \gamma_{\text{Fe}^{3+}} \times [\text{Fe}^{3+}](\text{concentration})$, and $IS = 0.5 \sum c_i z_i^2$. c_i is the

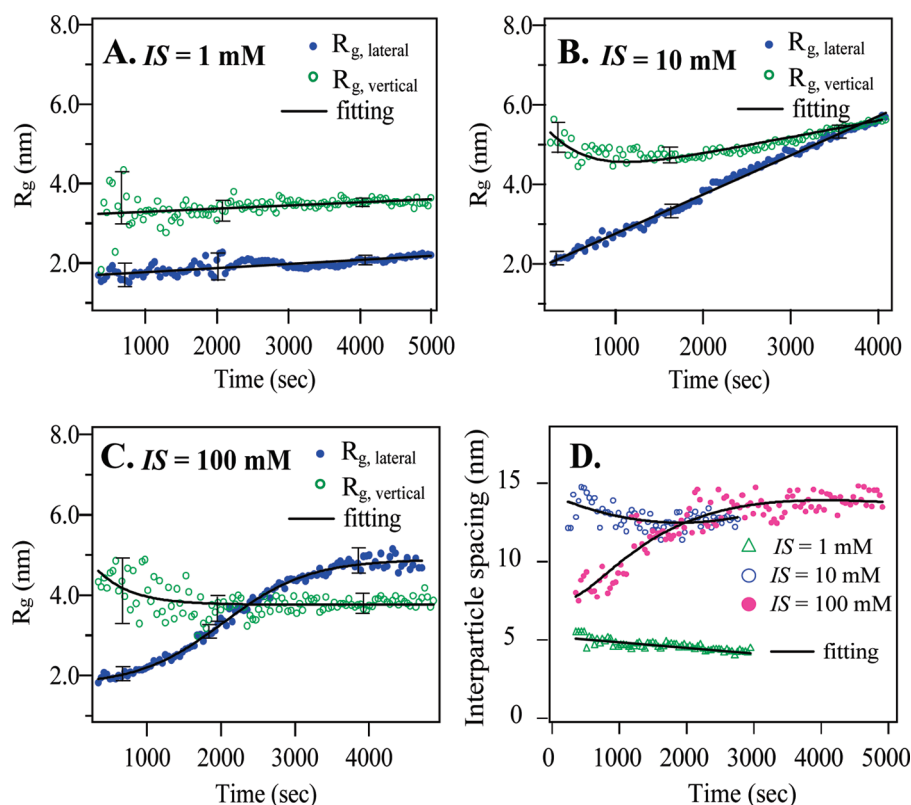


FIGURE 4. Sizes and interparticle spacings of iron oxide nanoparticles at different ionic strengths. $R_{g,lateral}$ and $R_{g,vertical}$ are the radii of particles in the surface plane and in the normal direction, respectively. (A) $[Fe^{3+}] = 0.1$ mM and $[NaNO_3] = 1$ mM; (B) $[Fe^{3+}] = 0.1$ mM and $[NaNO_3] = 10$ mM; (C) $[Fe^{3+}] = 0.1$ mM and $[NaNO_3] = 100$ mM; and (D) Interparticle spacings of nanoparticles as a function of IS. The solid lines depict the size trend.

molar concentration of ion i , and z_i is the charge number of that ion. A is 0.5085 in water at 25 °C. The ferric solution at 100 mM IS and pH 3.6 is 20% undersaturated with respect to ferrihydrite (Figure 5), although particle nucleation and growth was seen in our experiment. However, precipitation can occur if the ferric concentration near the surface is significantly higher than that in the solution (25), or if metastable iron oxyhydroxides, less stable than ferrihydrite ($Fe(OH)_3$), are formed that have lower nucleation activation energy barriers. The latter possibility suggests the initial formation of a highly disordered and likely hydrous phase (26).

Determination of the Smallest Nanoparticle Radii. Our approach using an in situ time-resolved simultaneous SAXS/GISAXS setup also allows determination of the smallest nanoparticle radii, which are assumed to be close to the critical nucleus size. There are few direct experimental approaches for determination of critical nucleus size, and most estimates have been derived from computer simulations (27). Using CNT, we can calculate the homogeneously nucleated critical nucleus size from the equation: $R_c = (2V_m\gamma_{wn})/(k_B T \ln \sigma)$ (28), where R_c is the critical nucleus radius, V_m is the volume per molecule based on ferrihydrite (10), γ_{wn} is the interfacial energy between water and iron oxide nanoparticles, k_B is the Boltzmann constant, T is the temperature, and σ is the saturation ratio, respectively. Because γ_{wn} is not available, the interfacial energy of goethite and water was used (1.6 J/m²) (29), and the ferric ion activities were used as derived with ferrihydrite as the reference phase. The calculated critical nucleus radii based on homogeneous nucleation are 21.1 and 31.5 nm at IS = 1 and 10 mM, respectively. At IS = 100 mM, the system is undersaturated and so no calculation is possible.

For calculation of the heterogeneous critical nucleus size, the effective specific energy, $\gamma_{ef} =$

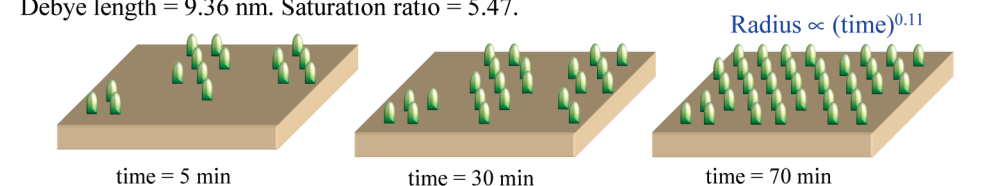
$\{(1/4)(2+\cos\theta)(1-\cos\theta)^2\}^{1/3}\gamma_{wn} = 0.91$ J/m², is calculated (30), where θ is the contact angle of the iron oxide nanoparticle and substrate, set here as 63.4° (diameter: height of nucleus = 1: 2). The interfacial energy term γ_{wn} has to be replaced by γ_{ef} , which reflects the interfacial response of the foreign substrate with respect to the nucleating phase (30). The calculated heterogeneous critical nucleus radii are 12.0 and 17.9 nm at IS = 1 and 10 mM, respectively. There is a caveat for these calculations. The interfacial energy of iron oxide/silicate combinations is presently not available and is difficult to measure. Hence, the calculated critical nucleus radii are likely only rough estimates, but do predict a 2-fold decrease in size for the heterogeneous nuclei. The observed nanoparticles can be smaller than the calculated critical nucleus sizes due to two reasons as previously described: First, locally high concentrations close to surfaces may drive faster formation and consequently smaller nucleus development. Second, if the nanoparticles are less stable than the iron oxide phase energies used in the calculations, then the critical nucleation size would be reduced due to the lower activation energy barrier for nucleation.

The direct measurements of the laterally smallest nucleus radii of iron oxide nanoparticles at quartz surfaces are 1.7 ± 0.3 , 1.8 ± 0.2 , and 1.7 ± 0.5 nm at IS = 1, 10, and 100 mM, respectively, which are values to extrapolated to time = 0. As particle scattering was not discernible above noise levels during the first 2–3 min, we assume that the system was in a prenucleation stage. Hence, the smallest nucleus sizes observed at the surface are likely near the critical nucleus size. These iron oxide critical nucleus sizes are consistent with the physical boundary condition, where iron oxide nanoclusters, precritical nuclei, pass the critical nucleus size by the hydrolysis of ferric ions (at $[OH]/[Fe^{3+}] \geq 2.5$ from ref 31).

At $IS = 1\text{ mM}$, more nucleation than growth.

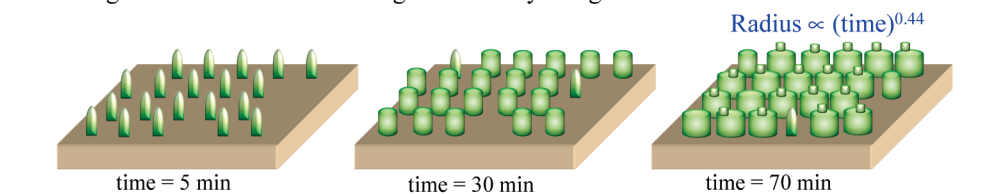
Limiting factor: Stronger repulsion between iron oxide monomers compared to others.

Debye length = 9.36 nm. Saturation ratio = 5.47.



At $IS = 10\text{ mM}$, active nucleation and growth occurs.

Limiting factor: No obvious limiting factor. Debye length = 2.96 nm. Saturation ratio = 3.12.



At $IS = 100\text{ mM}$, active nucleation and growth occurs.

Limiting factor: Diffusion-limited growth: depletion zone occurs.

Debye length = 0.96 nm. Saturation ratio = 0.80 (undersaturated).

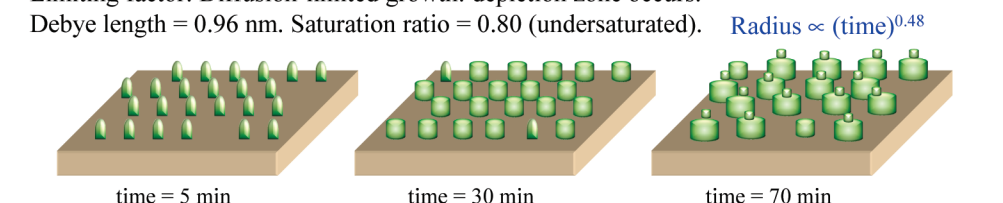


FIGURE 5. Proposed dominant mechanisms and topology of heterogeneous nucleation in ferric-quartz-water systems depending on IS . Different controlling influences dominate, depending on the IS . Debye length (= diffuse layer thickness) calculations are based on the following equation from ref 40: Diffuse layer thickness = $2.32 \times 10^9 (\sum c_i z_i^2)^{1/2}$. Saturation ratios ($\sigma = Q/K_{sp}$) with respect to ferrihydrite are provided. Q is the activity product and K_{sp} is the solubility product at equilibrium. For clarity, the contribution of the stepped surfaces are omitted in this diagram. The diagram shown here illustrates average nanoparticle nucleation and growth behavior in the sample surfaces.

Effects of Ionic Strength on Nucleation and Growth of Iron Oxides. Interestingly, the topology and kinetics of nucleation and growth of iron oxide nanoparticles at the same ferric concentration differ widely as a function of IS (Figures 3 and 4). Recalling the total particle volumes for heterogeneous nucleation in Figure 3, the maximum particle scattering occurred at 10 mM IS , with continuous particle size growth. At 1 mM IS , the nucleation of particles is active, but very slow growth occurs. The solution with 100 mM IS presented similar early stage growth to that of 10 mM IS . However, growth in particle size and volume slowed over time in comparison to that of the 10 mM IS . The lobes indicative of interparticle distance in the GISAXS images were most pronounced at 100 mM IS , indicating that nanoparticles at surfaces were well separated, with less coalescence than found at lower IS .

Three different effects could contribute to produce these observations. First, the substrate atomic structure and topology may control nucleation and growth. Although the experiments were conducted using the same types of substrates, it is possible that each sample may have had a different surface step density, crystallographic orientation, or other energetic differences (12, 32). To test this, we examined the (1102) surfaces of quartz in analogous experiments, but observed only a small difference in nanoparticle size. Hence, substrate structure and, by inference, topology, is not the main controlling factor. Second, electrostatic effects within the electrical double layer can influence nanoparticle formation pathways (33). However, if electrostatic interactions play the dominant role, then interparticle spacing (D in Figures 1A and 4D) at surfaces will decrease with increasing ionic strengths

due to electric double layer compression (34), but the observations indicate the opposite trend ($D_{1\text{ mM}} < D_{10\text{ mM}} < D_{100\text{ mM}}$, Figure 4D). Therefore, the potential contribution of electrostatic interaction between nanoparticles was ruled out in our experimental systems. Third, when IS increases, ferric ion activity can significantly decrease, and this can lead to a diffusion-limited nucleation and growth regime. For $IS = 100\text{ mM}$, the radius of iron oxide nanoparticles was proportional to $\text{time}^{0.48}$, consistent with diffusion-limited growth (Figure 5) (35). Under this condition, depletion zones are created around growing particles, leading to the well-defined interparticle spacings we observed (36). Hence, we infer that a combination of low ferric activity and fast nucleation and growth due to lower free energy of formation are the key controlling factors defining the different nucleation and growth behaviors as a function of IS .

Furthermore, secondary 0.8–1 nm radius particles were observed to develop at a later time and high IS (Figure 3C and D), while the growth of existing nanoparticles continued. These sizes are much smaller than the initial smallest nanoparticle radii. Such particles could represent the attachment of partially hydrolyzed ferric clusters to the existing nanoparticles because the size of the partially hydrolyzed ferric clusters are 0.7 nm at $[\text{OH}]/[\text{Fe}^{3+}] = 1.5$ from ref 31. In summary, the mechanistic and morphological understanding emerging from the current work is depicted in Figure 5.

Environmental Implications

Our study shows how a new in situ time-resolved SAXS/GISAXS technique allows accurate depiction of evolving

nanoparticle distributions and topology at an active interface, and yields improved dynamic morphological information unavailable with current molecular-scale imaging tools. Combined with thermodynamic analysis, our study reveals the complexity of nucleation and growth pathways during the early stage development, where nanoparticle–substrate interactions are dominant. Our findings have implications to any type of precipitation processes at solid–water interfaces. For example information about in situ reaction dynamics during geologic carbon sequestration, including morphology and porosity changes in geo-media after exposure to CO₂-rich saline solutions can be obtained under realistic pressures and temperatures and directly compared with simulations to test their veracity. In biomedical applications, monitoring of the stability and dissolution/precipitation of engineered nanomaterials at tissue/biological fluid interfaces (37, 38) is feasible, and could help understanding of the interactions and benignity of engineered nanomaterials to living cells. Finally, perhaps most importantly, real-time in situ monitoring of molecular species development on substrates constitutes a required element in the current scientific Grand Challenge (39) of green chemistry materials to control their structure, properties, and technological effectiveness.

Acknowledgments

Jun and Waychunas acknowledge funding from the joint NSF-DOE Environmental Molecular Science Institute at Pennsylvania State University, supported by the Department of Energy Office of Biological and Environmental Research. Jun acknowledges support from the International Center for Advanced Renewable Energy & Sustainability (I-CARES) at Washington University in St. Louis and from the Ralph E. Powe Junior Faculty Enhancement Award. We also thank Dr. Sönke Seifert at APS sector 12ID-C and Drs. Michael Toney and Thomas M. Weiss for help with SSRL beamline conditions and for useful discussions. Use of the Advanced Photon Source at Argonne National Laboratory was supported by the US Department of Energy, Office of Science, Office of Basic Energy Sciences, under Contract No. DE-AC02-06CH11357.

Supporting Information Available

Descriptions about sample size corrections in GISAXS intensity, four figures, and one table. This material is available free of charge via the Internet at <http://pubs.acs.org>.

Literature Cited

- Chan, C. S.; De Stasio, G.; Welch, S. A.; Girasole, M.; Frazer, B. H.; Nesterova, M. V.; Fakra, S.; Banfield, J. F. Microbial polysaccharides template assembly of nanocrystal fibers. *Science* **2004**, *303* (5664), 1656–1658.
- Moreau, J. W.; Weber, P. K.; Martin, M. C.; Gilbert, B.; Hutcheon, I. D.; Banfield, J. F. Extracellular proteins limit the dispersal of biogenic nanoparticles. *Science* **2007**, *316*, 1600–1603.
- Ganguli, P. M.; Mason, R. P.; Abu-Saba, K. E.; Anderson, R. S.; Flegal, A. R. Mercury speciation in drainage from the New Idria mercury mine, California. *Environ. Sci. Technol.* **2000**, *34* (22), 4773–4779.
- Jun, Y. S.; Kendall, T. A.; Martin, S. T.; Friend, C. M.; Vlassak, J. J. Heteroepitaxial nucleation and oriented growth of manganese oxide islands on carbonate minerals under aqueous conditions. *Environ. Sci. Technol.* **2005**, *39*, 1239–1249.
- Grolimund, D.; Borkovec, M.; Barmetter, K.; Sticher, H. Colloid-facilitated transport of strongly sorbing contaminants in natural porous media: A laboratory column study. *Environ. Sci. Technol.* **1996**, *30*, 3118–3123.
- Brant, J.; Labille, J.; Bottero, J. Y.; Wiesner, M. R., Nanoparticle transport, aggregation, and deposition. In *Environmental Nanotechnology: Applications and Impacts of Nanomaterials*; Wiesner, M. R., Bottero, J. Y., Eds.; McGraw-Hill: New York, 2007; pp 231–296.
- Roelands, C. P. M.; ter Horst, J. H.; Kramer, H. J. M.; Jansens, P. J. Analysis of nucleation rate measurements in precipitation processes. *Cryst. Growth Des.* **2006**, *6* (6), 1380–1392.
- Kasama, T.; Murakami, T. The effect of microorganisms on Fe precipitation rates at neutral pH. *Chem. Geol.* **2001**, *180*, 117–128.
- Jun, Y. S.; Martin, S. T. Cobalt alters the growth of manganese oxide film. *Langmuir* **2006**, *22*, 2235–2240.
- Navrotsky, A.; Mazeina, L.; Majzlan, J. Size-driven structure and thermodynamic complexity in iron oxides. *Science* **2008**, *319*, 1635–1638.
- Majzlan, J.; Navrotsky, A.; Schwertmann, U., III. Enthalpies of formation and stability of ferrihydrite (similar to Fe(OH)₃), schwertmannite (similar to FeO(OH)_{3/4}(SO₄)_{1/8}), and epsilon-Fe₂O₃. *Geochem. Cosmochim. Acta* **2004**, *68* (5), 1049–1059.
- Benning, L. G.; Waychunas, G. A., Nucleation, growth, and aggregation of mineral phases: Mechanisms and kinetic controls. In *Kinetics of Water-Rock Interaction*; Brantley, S. L.; Kubicki, J. D.; F., W. A., Eds.; Springer: New York, 2008; pp 259–333.
- Pouget, E. M.; Bomans, P. H. H.; Goos, J. A. C. M.; Frederik, P. M.; de With, G.; Sommerdijk, N. A. J. M. The initial stages of template-controlled CaCO₃ formation revealed by Cryo-TEM. *Science* **2009**, *323*, 1455–1458.
- Lee, B.; Seifert, S.; Riley, S. J.; Tikhonov, G.; Tomczyk, N. A.; Vajda, S.; Winans, R. E. Anomalous grazing incidence small-angle x-ray scattering studies of platinum nanoparticles formed by cluster deposition. *J. Chem. Phys.* **2005**, *123* (7), XXX.
- Renaud, G.; Lazzari, R.; Revenant, C.; Barbier, A.; Noblet, M.; Ulrich, O.; Leroy, F.; Jupille, J.; Borensztein, Y.; Henry, C. R.; Deville, J. P.; Scheurer, F.; Mane-Mane, J.; Fruchart, O. Real-time monitoring of growing nanoparticles. *Science* **2003**, *300* (5624), 1416–1419.
- Gullikson, E. X-Ray Interactions With Matter: Mirror Reflectivity. http://henke.lbl.gov/optical_constants/mirror2.html. Accessed July 30, 2008.
- Diz, H. R.; Novak, J. T.; Rimstidt, J. D. Iron precipitation kinetics in synthetic acid mine drainage. *Mine Water Environ.* **1999**, *18* (1), 1–14.
- Appelo, C. A. J.; De Vet, W. W. J. M., Modeling in situ iron removal from groundwater with trace elements such as As. In *Arsenic in Groundwater*; Welch, A. H. S., K. G., Ed.; Kluwer Academic Publishers: Boston, 2003; pp 381–401.
- Yoneda, Y. Anomalous surface reflection of X-rays. *Phys. Rev.* **1963**, *131* (5), 2010–2013.
- Lee, B.; Oh, W.; Yoon, J.; Hwang, Y.; Kim, J.; Landes, B. G.; Quintana, J. P.; Ree, M. Scattering studies of nanoporous organosilicate thin films imprinted with reactive star porogens. *Macromolecules* **2005**, *38* (22), 8991–8995.
- Ryan, J. N.; Elimelech, M. Colloid mobilization and transport in groundwater. *Colloids Surf., A* **1996**, *107*, 1–56.
- Janicki, J. SAXS and WAXD real time studies on nanostructure of selected polymer materials. *J. Alloys Compd.* **2004**, *382* (1–2), 61–67.
- Schecher, W. D.; McAvoy, D. C. MINEQL+: A Chemical Equilibrium Modeling System, Version 4.5; Environmental Research Software: Hallowsell, ME, 1998.
- Stumm, W.; Morgan, J. J. *Aquatic Chemistry*; Wiley: New York, 1996.
- Srivastava, A.; Muralidhar, K.; Panigrahi, P. K. Measurement of three-dimensional concentration gradients around a crystal growing from its aqueous solution using laser schlieren. *Cryst. Res. Technol.* **2007**, *42*, 778–790.
- Navrotsky, A. Energetic clues to pathways to biomineralization: Precursors, clusters, and nanoparticles. *Proc. Natl. Acad. Sci. U.S.A.* **2004**, *101* (33), 12096–12101.
- Pan, A. C.; Rappl, T. J.; Chandler, D.; Balsara, N. P. Neutron scattering and Monte Carlo Determination of the variation of the critical nucleus size with quench depth. *J. Phys. Chem. B* **2006**, *110*, 3692–3696.
- De Yoreo, J. J.; Vekilov, P. G. Principles of crystal nucleation and growth. *Rev. Mineral. Geochem.* **2003**, *54*, 57–93.
- Steeff, C. I.; Van Cappellen, P. A new kinetic approach to modeling water-rock interaction: The role for nucleation, precursors, and Ostwald ripening. *Geochim. Cosmochim. Acta* **1990**, *54*, 2657–2677.
- Kashchiev, D.; van Rosmalen, G. M. Review: Nucleation in solutions revisited. *Cryst. Res. Technol.* **2003**, *38* (7–8), 555–574.
- Bottero, J. Y.; Tchoubar, D.; Arnaud, M.; Quienne, P. Partial hydrolysis of ferric nitrate salt. structural investigation by dynamic light scattering and small-angle X-ray scattering. *Langmuir* **1991**, *7*, 1365–1369.

- (32) Jun, Y. S.; Martin, S. T. Microscopic observations of reductive manganite dissolution under oxic conditions. *Environ. Sci. Technol.* **2003**, *37* (11), 2363–2370.
- (33) Kemps, J. A.; Bhattacharjee, S. Interactions between a solid spherical particle and a chemically heterogeneous planar substrate. *Langmuir* **2005**, *21*, 11710–11721.
- (34) Gilbert, B.; Lu, G.; Kim, C. S. Stable cluster formation in aqueous suspensions of iron oxyhydroxide nanoparticles. *J. Colloid Interface Sci.* **2007**, *313* (1), 152–159.
- (35) Lasaga, A. C. *Kinetic Theory in the Earth Sciences*; Princeton University Press: Princeton, NJ, 1998; p 497–712.
- (36) Vilaseca, E.; Trigueros, P. P.; Garces, J. L.; Mas, F. A computer simulation model for the diffusion controlled nucleation and growth processes on electrode surfaces—A two-dimensional study. *J. Electroanal. Chem.* **1998**, *458*, 55–72.
- (37) Borm, P.; Klaessig, F. C.; Landry, T. D.; Moudgil, B.; Pauluhn, J.; Thomas, K.; Trotter, R.; Wood, S. Research strategies for safety evaluation of nanomaterials, Part V: Role of dissolution in biological fate and effects of nanoscale particles. *Toxicol. Sci.* **2006**, *90* (1), 23–32.
- (38) Limbach, L. K.; Wick, P.; Manser, P.; Grass, R. N.; Bruinink, A.; Stark, W. J. Exposure of engineered nanoparticles to human lung epithelial cells: Influence of chemical composition and catalytic activity on oxidative stress. *Environ. Sci. Technol.* **2007**, *41* (11), 4158–4163.
- (39) Omenn, G. S. Grand challenges and great opportunities in science, technology, and public policy. *Science* **2006**, *314*, 1696–1704.
- (40) Elimelech, M.; Gregory, J.; Jia, X.; Williams, R. A., *Particle Deposition and Aggregation—Measurement, Modelling and Simulation*; Butterworths-Heinemann: Woburn, MA, 1995.

ES101491E